Wu *et al. Energy Mater.* **2025**, *5*, 500055
DOI: 10.20517/energymater.2024.164

Energy Materials

Article

Open Access

Check for updates

Mechanochemical process enhancing pore reconstruction for dense energy storage of carbon-based supercapacitors

Dongyang Wu[1], Fei Sun[1,*], Hua Wang[1], Yang Li[2], Boran Zhang[1], Chenglong Yang[2], Zhefan Wang[2], Jihui Gao[1], Guangbo Zhao[1]

[1]School of Energy Science and Engineering, Harbin Institute of Technology, Harbin 150001, Heilongjiang, China.
[2]Xi'an Thermal Power Research Institute Co., Ltd, Xi'an 710054, Shaanxi, China.

***Correspondence to:** Dr. Fei Sun, School of Energy Science and Engineering, Harbin Institute of Technology, No. 92 Xidazhi Street, Nangang District, Harbin 150001, Heilongjiang, China. E-mail: sunf@hit.edu.cn

How to cite this article: Wu, D.; Sun, F.; Wang, H.; Li, Y.; Zhang, B.; Yang, C.; Wang, Z.; Gao, J.; Zhao, G. Mechanochemical process enhancing pore reconstruction for dense energy storage of carbon-based supercapacitors. *Energy Mater.* **2025**, *5*, 500055. https://dx.doi.org/10.20517/energymater.2024.164

Received: 7 Sep 2024 **First Decision:** 26 Oct 2024 **Revised:** 12 Nov 2024 **Accepted:** 18 Nov 2024 **Published:** 25 Feb 2025

Academic Editor: Yuping Wu **Copy Editor:** Fangling Lan **Production Editor:** Fangling Lan

Abstract

Improving the volumetric energy density of carbon electrode materials for supercapacitors is of significance to reducing the size of energy storage devices, and eliminating the ineffective pores in porous carbon electrode materials is the key to achieving dense storage of ions. Herein, we reconstruct the pore structure of commonly activated carbon via a facile high-energy mechanochemical process, by which modified activated carbon exhibits a much-increased packing density with an ultra-low specific surface area of 33 $m^2 g^{-1}$ without sacrificing the gravimetric specific capacitances, thereby enabling high volumetric capacitances up to 602 F cm^{-3}. Gas adsorption characterization and small angle X-ray scattering tests collectively reveal the regulatory mechanism of mechanochemical process on pore structure reconstruction that high-energy mechanochemical treatment significantly eliminates the excess meso-/macro-pore volume to configure a compressed carbon skeleton structure and simultaneously increases proportions of micropore volume in the total pore volume, ultimately resulting in a cross-linked dense pore network structure. Benefitting from the optimized pore network and oxygen atoms introduced by mechanochemistry, the assembled aqueous symmetric supercapacitor in KOH electrolyte delivers a maximum volumetric energy density of 11.32 Wh L^{-1} when the volumetric power density is 223 W L^{-1}. This work systematically reveals the effects of mechanical force on the pore reconstruction of carbon materials, and provides a simple method for enhancing the volumetric performances of carbon-based porous electrode materials.

Keywords: Activated carbon, mechanochemistry, pore reconstruction, volumetric capacitance, carbon-based supercapacitors

INTRODUCTION

Carbon materials are widely used as supercapacitor electrodes because of their tunable multi-scale structure[1-5]. The ion storage and transport mechanisms are closely related to the porous structure of electrode materials. In previous studies, increasing the specific surface area of carbon materials has been regarded as an effective strategy to improve the capacitances of electrical double-layer supercapacitors. Therefore, using coal[6,7], biomass[8,9] and polymers[10] as carbon precursors, porous carbon with a high specific surface area prepared by the activation method is commonly used for supercapacitor electrodes. However, the high porosity and packing density of porous carbon are often contradictory, resulting in a low volumetric energy density of porous carbon materials, which is not conducive to reducing device sizes. Specifically, commercial activated carbon used for supercapacitors usually provides a gravimetric capacitance of 200 F g^{-1}, while the volumetric capacitance is commonly lower than 200 F cm^{-3} due to the low packing density caused by rich porosity. In addition, methods for preparing porous carbon materials such as template method[11-13], vapor deposition[14-16] and *in-situ* bottom-up synthesis[17-19] all face the bottleneck of balancing gravimetric and volumetric energy density simultaneously. Optimizing the pore structure of porous carbon to achieve dense ion storage is the key to improving the volumetric performances of carbon-based electrodes and supercapacitors.

For common activated carbon electrode materials, pores often exhibit disordered or chaotic distribution, and not all of them are conducive to ion storage and transport. It has been widely accepted that the micropores in porous carbon are considered to be effective ion storage sites[20], while the meso-/macro-pores act as ion transport channels, which facilitate the rapid diffusion of electrolyte ions[21]. Therefore, hierarchical porous carbon is considered to be the preferred structure for achieving rapid ion transport and storage[5,22-24]. Furthermore, the researchers believe that when the pore diameter is close to the ion size, ions in the electrodes can achieve high-density storage due to the confinement behavior of the pore wall[25]. Therefore, many strategies such as adopting graphene-based raw materials[26-28], using solvent tension and capillary condensation[29], or preparing composite materials[30,31] have been explored to optimize the pore structure distribution and improve the material density. However, these methods generally involve complex preparation processes and costly raw materials, and it is difficult to adjust and reconstruct the pore structure that has been formed in the materials. In addition, the current research consensus is that the closed pores do not contribute to the ion storage capacity[32,33], but occupy the space and lead to low density. Therefore, it is highly desirable to develop a simple post-treatment strategy to eliminate ineffective pores by deeply adjusting and modifying the pore structure already formed in porous or activated carbon.

Ball milling technology is mainly used in industry as a means of particle refinement or homogenization through the strike, friction and rolling between the balls and the materials under the action of mechanical force[34]. In recent years, mechanochemistry has been found to play a role in micro-nano scale structure regulation of carbon materials, such as heteroatom doping or microcrystalline structure modulation. For example, a mechanochemically-assisted method has been reported for preparing B, N co-doped porous carbon, and the mechanical action facilitates the homogeneous dispersion of B and N dopants into the whole composite due to the hydrogen-bond interaction[35,36]. In addition, smaller and thinner graphitic-like nanodomains and more disorder structure can be obtained by mechanical ball milling of hard carbon. Previous research by our team found that the CO_2-assisted mechanical ball milling method can achieve precise doping of carboxyl groups in the microcrystalline structure of carbon materials and high reversible capacity storage of sodium ions[37]. In the mechanochemical process, grinding, shearing and other forces can be introduced to break the chemical bonds on the surface of the material, while the local transient high

temperature is generated, which contributes to the diffusion of microcrystalline defects and the rearrangement of atoms[38-40]. Therefore, it can be expected that the energy provided by the mechanochemical process can cause the pore walls of the activated carbon to collapse, and further lead to the rearrangement of the pore structure through the recombination of unsaturated bonds, so as to achieve the deep adjustment of the pore structure.

In this work, we demonstrate for the first time that a convenient mechanochemical post-engineering approach can reconfigure and optimize the pore structure and doping environment of traditional activated carbon, thereby achieving a significant increase in the volumetric performances of carbon-based electrodes and supercapacitors. Specifically, a cost-effective, low-grade coal precursor was first physically activated to prepare porous carbon, which was then experienced a sealed ball milling procedure to achieve porosity regulation. Notably, mechanochemistry (high-energy ball milling) can significantly increase the material skeleton density of activated carbon from 1.0[3] to 1.79 g cm^{-3} by reducing porosity, specific surface area and pore volume, and the reduced pores are mainly ineffective ones. The obtained modified carbon maintained high gravimetric specific capacitances of 337 F g^{-1}. Gas adsorption and desorption characterizations, SAXS tests and closed pore analysis collectively revealed the evolution of the pore structure of activated carbon by mechanochemical treatment. As the ball milling process proceeded, the proportions of micropore volume in the total pore volume increased, and the ineffective intergranular meso-/macro-pores and intragranular closed pores were significantly eliminated followed by intragranular pores further development and reorganization, ultimately forming more cross-linked dense porous network structure. In addition, the mechanochemical process introduces oxygen atoms into the carbon matrix to provide extra pseudocapacitances. Benefiting from the increased packing density, the optimized porosity and introduced oxygen atoms, the obtained dense carbon demonstrates excellent volumetric specific capacitances up to 602 F cm^{-3}. The constructed aqueous symmetric supercapacitor with 6M KOH electrolyte delivers a maximum volumetric energy density of 11.32 Wh L^{-1} when the volumetric power density is 223 W L^{-1}.

EXPERIMENTAL SECTION

Preparation of CAC and CAC-*x*

Baorixile lignite was selected as raw coal for subsequent activation. Pulverized coal was sieved into 160-200 mesh (74-96 μm) followed by one-step activation at 800 °C for 1 h under the composite atmosphere containing CO_2 and N_2, in which the concentration of CO_2 was 40 vt-%. The obtained products were washed in HCl (5 mol L^{-1}) and HF (10 wt-%) to remove the ash components. The obtained CO_2-activated carbon (CAC) was then subjected to mechanical ball milling process in an agate tank with a rotation rate of 500 r/min, and the ratio of balls to materials was 50 to 0.1 g. The obtained samples after ball milling were noted as CAC-*x*, where *x* is the ball milling time. To remove the oxygen atoms in the materials, the samples of CAC, CAC-4 and CAC-24 were annealed at 800 °C for 1h in a hydrogen-argon mixture atmosphere, and the products were noted as CAC-H, CAC-4H and CAC-24H, respectively.

Material characterization

The field-emission scanning electron microscope (FE-SEM, Hitachi SU8010, Japan) and transmission electron microscope (TEM, FEI Tecnai G2 F20) were used to obtain the morphology and microstructure characteristics of the samples. Particle size distribution was measured by a laser particle analyzer (Malvern Mastersizer 2000). Information about the microcrystalline structure was gathered through X-ray diffraction (XRD) and Raman testing. The XRD patterns were recorded using a Panalytical Empyrean Intelligent X-ray diffractometer equipped with Cu Kα radiation (operating at 40 kV, 100 mA, with a wavelength of 1.54178 Å) on a Rigaku UltimaIV system. Meanwhile, Raman spectra were acquired using a Renishaw inVia confocal Raman system, employing a 50× objective lens with a numerical aperture of 0.75, and a laser power set at 0.15 mW with a wavelength of 532 nm. The material's carbon and oxygen element content was determined

through X-ray photoelectron spectroscopy (XPS) analysis, utilizing an Al Kα radiation source on a Thermo Scientific K-Alpha instrument. The pore structure was tested by N_2 adsorption-desorption installation, CO_2 adsorption-desorption installation and SAXS device. At 77 K, nitrogen isotherms were conducted using the BSD-PM2 surface area and a microporous analyzer manufactured by Beishide Instrument Technology (Beijing) Co., Ltd. At 273.15 K, carbon dioxide isotherms were performed using Quantachrome Instruments software version 3.0. The Brunauer-Emmett-Teller equations were utilized to calculate the specific surface area, while the pore size distribution was derived using the nonlocal density functional theory approach. SAXS was measured by Anton Paar SAXSess MC2 using a copper target light tube (λ = 0.1542 nm), operating at 40 kV and 40 mA. A little sample was filled in Paste Cell, sealed and put into the sample holder of the instrument. After vacuuming to 10 Pa, the measurement of small-angle X-ray scattering was performed at 25 °C for 20 min.

Electrode fabrication and electrochemical measurements

For the preparation of the testing electrode, a mixture of CAC-*x*, carbon black, and poly(tetrafluoroethylene) in a mass ratio of 8:1:1 was compressed onto a nickel foam current collector (suitable for the three-electrode system and symmetrical aqueous electrolyte system) or aluminum foil (appropriate for the ionic liquid electrolyte system). The electrode was then dried in a vacuum oven at 110 °C for a duration of 12 h. The active mass is about 0.8 mg for each single electrode. All electrochemical measurements were conducted at room temperature using a Bio-Logic VMP3 workstation. In the standard three-electrode configuration, the synthesized sample served as the working electrode, the saturated calomel electrode (SCE) as the reference electrode, and a Pt foil as the counter electrode. A 6M KOH aqueous solution served as an electrolyte at room temperature. Cyclic voltammetry (CV) measurements were conducted at various scanning rates, while galvanostatic charge/discharge (GC) curves were recorded at different current densities. The gravimetric capacitances could be derived from the CV curves using

$$C_g = \frac{\int i dV}{2mvV} \ (\mathrm{F\ g^{-1}}) \tag{1}$$

where C_g stands for gravimetric specific capacitance (F g^{-1}), the variable i represents the response current (A), v denotes the potential scan rate (V s^{-1}), V corresponds to the range of applied voltage (V), and m represents the mass of active material on each electrode (g).

The gravimetric capacitances can alternatively be derived from the GC curves using

$$C_g = \frac{I\Delta t}{m\Delta V} \ (\mathrm{F\ g^{-1}}) \tag{2}$$

in which I represents the constant charge/discharge current (A), Δt stands for the discharge time (s), m is the weight of active material (g), and ΔV refers to the voltage range during the discharging process, excluding the potential drop (V).

The skeleton density reflects the density of the active material when accounting for pore volume, as calculated by

$$\rho_M = \frac{1}{V_T + 1/\rho_T} \ (\mathrm{g\ cm^{-3}}) \tag{3}$$

where ρ_M is material skeleton density (g cm^{-3}), V_T refers to the total pore volume (cm^3 g^{-1}) measured by nitrogen adsorption, and ρ_T indicates the true density of carbon (2.0 g cm^{-3})[41,42].

The volumetric capacitances can be calculated using

$$C_v = C_g \times \rho_M \text{ (F cm}^{-3}\text{)} \tag{4}$$

where C_v is volumetric specific capacitance (F cm^{-3}).

The symmetric aqueous supercapacitors were built in the CR2032 coin-type cell using two equal electrodes (with nickel foam current collector), a glassy fibrous separator and 6M KOH electrolyte (voltage range of 0-1.0 V). For the $EMIMBF_4$ ionic liquid electrolyte, the symmetric supercapacitors were constructed utilizing two identical electrodes with NKK-TF4030 as a separator and aluminum foil as a current collector. These devices were tested in a two-electrode cell configuration with a voltage range spanning from 0 to 3.6 V. The specific capacitance of the symmetric supercapacitor was calculated from the galvanostatic discharge curve according to

$$C_s = 2\times\frac{I\Delta t}{m\Delta V} \text{ (F g}^{-1}\text{)} \tag{5}$$

where I represents the constant charge/discharge current (A), Δt is the discharge time (s), m is the mass of a single electrode (g), and ΔV is the discharging potential range excluding any potential drop (V).

The energy density and power density of symmetric supercapacitors were calculated using

$$E_g = \frac{1}{8}\times\frac{1}{3.6}C_s V^2 \text{ (Wh kg}^{-1}\text{)} \tag{6}$$

$$P_g = \frac{E}{t}\times 3600 \text{ (W kg}^{-1}\text{)} \tag{7}$$

where E_g refers to gravimetric energy density (Wh kg^{-1}), V represents the working voltage of the cell (V), and t denotes the discharge time (s). Correspondingly, the volumetric performances were calculated by

$$E_v = E_g \times \rho_M \text{ (Wh L}^{-1}\text{)} \tag{8}$$

$$P_v = P_g \times \rho_M \text{ (W L}^{-1}\text{)} \tag{9}$$

Additionally, the compressed electrode density under a pressure of 10 MPa within a cylindrical mold reflects the compaction potential of the electrode in practical applications, and can also be calculated using

$$\rho_E = \frac{m}{h\times\pi\times r^2} \text{ (g cm}^{-3}\text{)} \tag{10}$$

in which m denotes the total mass of the electrode, which comprises the active materials, binder, and conductive agent (g); h represents the thickness of the electrode (cm), and r signifies the radius of the electrode (cm).

RESULTS AND DISCUSSION

Preparation and multi-scale structure characterization of CAC-*x*

The schematic illustration from a coal precursor to CAC and CAC-*x* is depicted in Figure 1A. First, the crushed lignite was physically activated to obtain the pristine CAC under a composite atmosphere of CO_2 and N_2. Afterward, the obtained CAC experienced the mechanochemical process to achieve porosity regulation, and the carbon materials obtained at different ball milling times were denoted as CAC-*x*. The following physicochemical structure characterization and comparative analyses elucidate the deep adjustment effects of mechanochemistry on the multi-scale structure of activated carbon. As shown in Figure 1B and Supplementary Figure 1, the pristine activated carbon CAC appears to block morphology with irregular rough textures on the surface of the particles, which may be caused by CO_2 gas etching. After the post-treatment of mechanical ball milling, significant differences can be seen in the particle size and dispersion morphology with the extension of ball milling time. When the activated carbon experienced short-time ball milling such as one or 4 h, the average size of particles decreased significantly, as can be seen in Figure 1C and Supplementary Figures 2 and 3. With the extension of ball milling time, there is a significant agglomeration phenomenon between particles, resulting in uneven particle size and reduced dispersion. Figure 1D shows the morphological characteristics of the CAC-24 sample, from which compared to CAC-4, the particle size becomes larger due to the agglomeration, and some smaller particles adhere to the surface of the larger ones. As can be seen in Supplementary Figures 4-7, similar results can be obtained for samples with ball milling time of more than 8 h. With the extension of milling time, the agglomeration degree of particles becomes higher, resulting in larger average particle sizes. The ball milling process not only significantly changes the particle size, but also affects the microcrystalline structure. Figure 1E-G, Supplementary Figures 8 and 9 show the effects of mechanochemical process on microcrystalline structure of activated carbon. Overall, the microcrystalline structure of all samples exhibits an amorphous state, and the anisotropy of microcrystalline lattices increases with the extension of ball milling time. To be specific, a high-resolution transmission electron microscopy (HRTEM) image in Figure 1E shows an isotropic microcrystalline structure for CAC, in which the microcrystalline lattices are distributed in short order, and the enclosed regions between microcrystals form the closed pores[43]. As the ball milling proceeds, a partially disordered microcrystalline structure gradually becomes ordered with increased microcrystalline size. For CAC-24 which experienced the longest ball milling time, certain regions of the microcrystals exhibit long-range ordered structure with a decrease in the content of closed pores.

To further reveal the influences of mechanochemistry on particle aggregation morphology, particle size distribution characteristics of CAC and CAC-*x* were characterized, as shown in Figure 1H and I. As can be seen, the particle size distribution of pristine CAC presents a normal distribution and the cumulative particle size distribution of 50% (D50) is 12 μm. When the milling time is extended to 4 h, particle size no longer exhibits a concentrated distribution but rather a multimodal distribution. The D50 particle sizes for CAC-1 and CAC-4 are calculated to be 1.40 and 0.95 μm, showing a precipice decline compared to CAC. Further extending the ball milling time to 24 h, the particle size distribution shows unimodal normal distribution again with the D50 particle sizes for CAC-24 increasing to 8.67 μm, which can be ascribed to the cold-welding between small particles and agglomeration into larger ones[44]. On the whole, the above morphology and particle size characterizations suggest that with the introduction of ball milling process and the extension of ball milling time, the size of activated carbon particles does not decrease monotonically, but rather involves the aggregation and recombination of smaller particles, which will cause profound changes in the pore structure of activated carbon. In addition to the variations in particle size and uniformity, the tap densities of activated carbon have also been changed during the ball milling process. The volume of 0.07 g CAC and CAC-*x* samples after vibration is shown in Figure 1J and Supplementary Figure 10. Compared to the pristine CAC, the tap density of CAC-24 has been greatly increased by nearly twice.

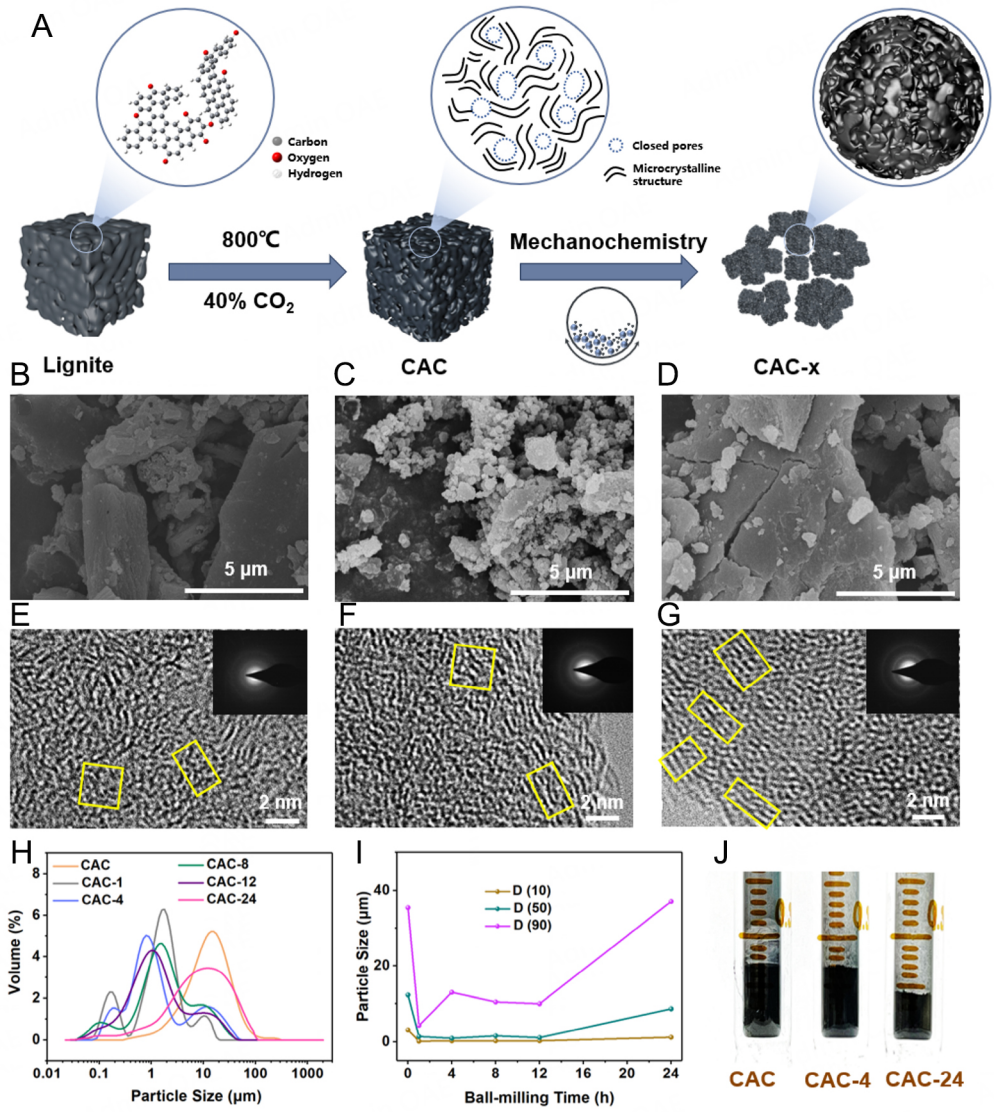

Figure 1. Preparation and structure characterizations. (A) Schematic illustration of the synthesized procedure of CAC-*x*. (B) SEM image of CAC. (C) SEM image of CAC-4. (D) SEM image of CAC-24. (E) TEM image of CAC. (F) TEM image of CAC-4. (G) TEM image of CAC-24. (H and I) Particle size distribution of CAC-*x* measured by laser particle analyzer. (J) The volume of 0.07 g CAC and CAC-*x* samples after vibration.

To gain deeper insights into the carbon microcrystalline characteristics resulting from the mechanochemical process, we conducted XRD and Raman spectroscopy tests. Supplementary Figure 11 and Figure 2A depict the overall and deconvoluted XRD patterns of CAC and CAC-*x* samples, respectively. The two broad diffraction peaks observed correspond to the (*002*) and (*100*) planes of a non-graphitized isotropic carbon structure[45]. The asymmetric (*002*) peak can be further decomposed into a γ-band subpeak at approximately 20°, indicative of a less-developed crystalline structure with a higher number of aliphatic carbon atoms, and an H-band subpeak at about 26°, indicative of a more-developed crystalline structure with a higher number of aromatic carbon atoms[46,47]. Based on these patterns, we calculated the microcrystalline parameters, including interlayer spacing (d_{002}), lateral size (L_a), and stacking height (L_c) for CAC and CAC-*x* samples, using the Bragg and Scherer equations [Supplementary Figure 12 and Supplementary Table 1]. On the whole, peaks (*002*) of CAC-*x* in the XRD curves become sharper with the

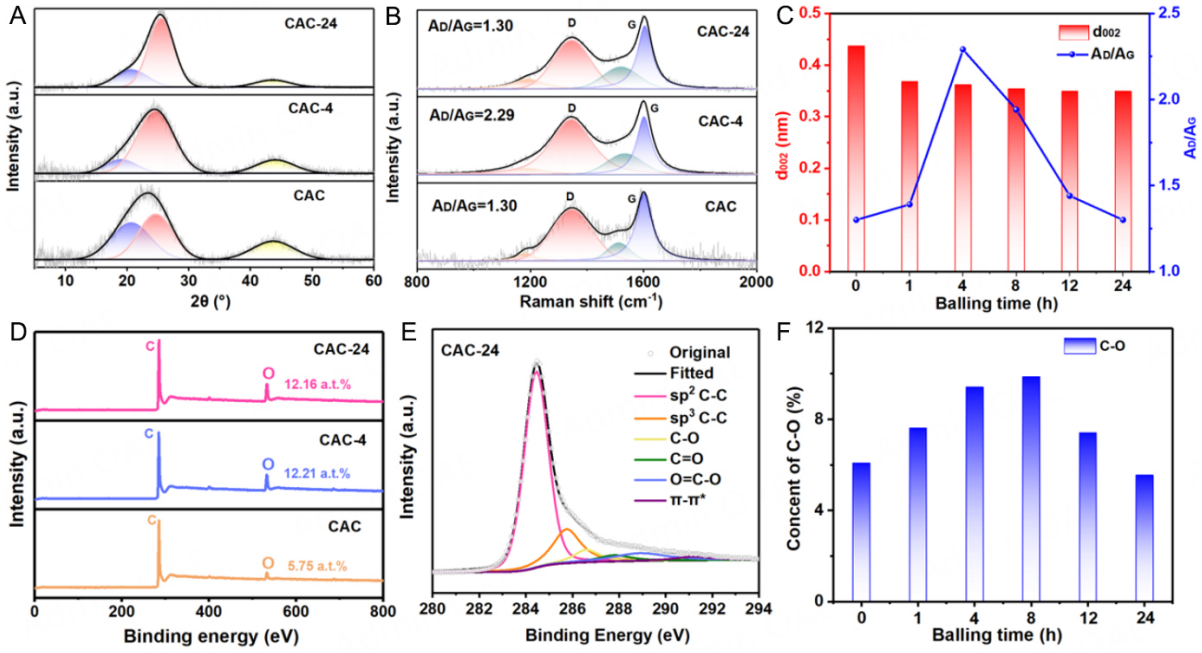

Figure 2. Microcrystalline and surface chemical structure characterization. (A) XRD patterns of CAC, CAC-4 and CAC-24. (B) Raman spectra of CAC, CAC-4 and CAC-24. (C) The values of d_{002} and A_D/A_G of CAC-*x*. (D) XPS overall scans of CAC, CAC-4 and CAC-24. (E) Deconvoluted *C1s* spectra of CAC-24. (F) The content of C-O of CAC-*x*.

extension of ball milling time, and the d_{002} values decrease significantly, which is attributed to the progressively increasing degree of graphitization. Specifically, d_{002} parameter for CAC is calculated to be 0.437 nm, while for CAC-4 and CAC-24 the values are 0.362 and 0.349 nm, respectively. These results align well with the values obtained from the HRTEM analysis in Figure 1E-G and Supplementary Figure 9.

As illustrated in Figure 2B, Supplementary Figures 13 and 14, the Raman spectra of CAC-*x* exhibit two prominent peaks that can be precisely decomposed into four subpeaks. Specifically, the *T* band centered at approximately 1,200 cm^{-1} corresponds to the A_{1g} breathing mode of an sp^2-sp^3 hybrid structure or C-C/C=C stretching vibrations. The D band at about 1,350 cm^{-1} represents the A_{1g} breathing mode of a disordered graphite lattice. The D_3 band at roughly 1,500 cm^{-1} indicates an organic molecular amorphous structure, while the G band at approximately 1,580 cm^{-1} is associated with the E_{2g} stretching vibration mode of a graphite lattice[48-50]. By calculating the area ratio of the D band to the G band (A_D/A_G), it is observed that CAC-4 exhibits a higher A_D/A_G value (2.29) compared to CAC (1.30). This may be due to the introduction of oxygen-containing functional groups during the ball milling process, as described in detail subsequently. However, the trend reverses when the ball milling time lasts longer [Figure 2C and Supplementary Table 2]. The A_D/A_G value of CAC-8 decreases to 1.94 and continues to decline to 1.30 for CAC-24. This may be because the content of oxygen-containing functional groups is almost constant after longer ball milling time, while microcrystalline layer spacing is gradually reduced. To gain further insight into the variations in the concentration of oxygen-containing functional groups during the mechanochemical process, XPS analyses were conducted. Figure 2D and Supplementary Figure 15 display the XPS survey scans of CAC and CAC-*x* samples, revealing distinct C1s and O1s signals. As indicated in Supplementary Table 3, as the ball milling duration increases, the content of oxygen-containing functional groups exhibits an upward trend, rising from 5.75 at.% for CAC to 12.21 at.% for CAC-4. This elevated content remains relatively stable, with similar values of 12.33 at.% for CAC-8, 12.38 at.% for CAC-12, and 12.16 at.% for CAC-24. The high-resolution C1s spectra [Figure 2E and Supplementary Figure 16] of the samples can be decomposed into six

subpeaks, each representing distinct configurations of oxygen doping within the carbon matrix. These configurations include the C-C sp^2 peak (284.7 eV), C-C sp^3 peak (285.4 eV), C-O peak (286.2 eV), C=O peak (287.3 eV), O-C=O peak (288.9 eV), and π-π^* transition peak (291.2 eV)[51-53]. As shown in Figure 2F, the content of C-O functional groups shows a trend of increasing first and then decreasing, which is consistent with the changing trend of A_D/A_G. This is mainly attributed to the strong collision between the balls and the carbon materials, which produces many highly active sites at the edges of the microcrystalline structure, and these sites are oxidized in the air to form oxygen-containing functional groups[44]. With the extension of ball milling time, the mechanical cold-welding process causes the microcrystalline structure recombination, and the oxygen atoms originally at the edges of the structure may be eliminated or released in the form of gas during the recombining process, resulting in a decrease in C-O content.

The storage behavior of ions in the carbon electrode of supercapacitors is closely related to the pore structure. In order to study the pore structure evolution of activated carbon during mechanochemical treatment, we adopted gas adsorption-desorption tests and SAXS characterizations. The porosity development of CAC-*x* influenced by ball milling time is illustrated through the N_2 adsorption-desorption isotherms and pore diameter distribution curves presented in Figure 3A and B, Supplementary Figure 17. Among the six tested samples, pristine CAC demonstrates the highest porosity, characterized by a specific surface area of 605 $m^2 g^{-1}$ and a pore volume of 0.5 $cm^3 g^{-1}$ [Supplementary Table 4], which is the typical pore characteristic of CAC. With the extension of ball milling time, the obtained CAC-*x* samples exhibit gradually decreased porosity and pore parameters (specific surface area and pore volume). For CAC-24, the specific surface area is only 33 $m^2 g^{-1}$ with the pore volume of 0.06 $cm^3 g^{-1}$ based on N_2 adsorption-desorption test. As shown in Figure 3A and Supplementary Figure 17, when the milling time is short (1~8 h), the N_2 adsorption content with P/P_0 below 0.15 which refers to intragranular pore[54] has a slight reduction for CAC-1, CAC-4 and CAC-8, but for the range of P/P_0 above 0.15 which refers to interparticle pore[54], there is a significant decrease. It is indicated that the short-time ball milling process mainly changes interparticle porosity, and has limited effect on the internal porosity of the particles. However, for CAC-12 and CAC-24, both the N_2 adsorption content with P/P_0 below and above 0.15 was significantly reduced, indicating that long-time ball milling has an important effect on both intergranular and intragranular pores of activated carbon.

In order to further obtain a smaller-scale micropore evolution picture, CO_2 adsorption-desorption tests have been performed. As shown in Figure 3C and Supplementary Figure 18, the calculated specific surface area and pore volume of the samples slightly increase after short-time ball milling compared with the pristine CAC based on CO_2 adsorption-desorption tests (specifically, 537 $m^2 g^{-1}$ and 0.151 $cm^3 g^{-1}$ for CAC and 647 $m^2 g^{-1}$ and 0.187 $cm^3 g^{-1}$ for CAC-4). However, the specific surface area and pore volume of CAC-24 obtained with longer milling time decreased significantly compared to CAC. In addition, it can be seen from Figure 3D and Supplementary Figure 18 that the micropore size distribution curves of all samples exhibit a trimodal distribution, indicating that the samples mainly contain three kinds of micropores with diameters of 0.38, 0.50 and 0.80 nm. Furthermore, based on the N_2 and CO_2 adsorption characterizations, the sum of the micropore volume (V'_{micro}) obtained by CO_2 adsorption and the meso-/macro- pore volume ($V_{macro\text{-}meso}$) obtained by N_2 adsorption was calculated as the total pore volume (V'_{total}) of the samples, and the ratios of micropore volume to the total pore volume of the samples were further calculated. As shown in Figure 3E and Supplementary Table 4, the ratios increase gradually with ball milling time.

To further explore the effects of ball milling process on the closed pores inside the activated carbon, the true densities of CAC-*x* were tested, by which the volume of the closed pores can be calculated. As shown in Figure 3F, as the milling time extends, the true densities of CAC-*x* gradually increase (from 0.63 g cm^{-3} for

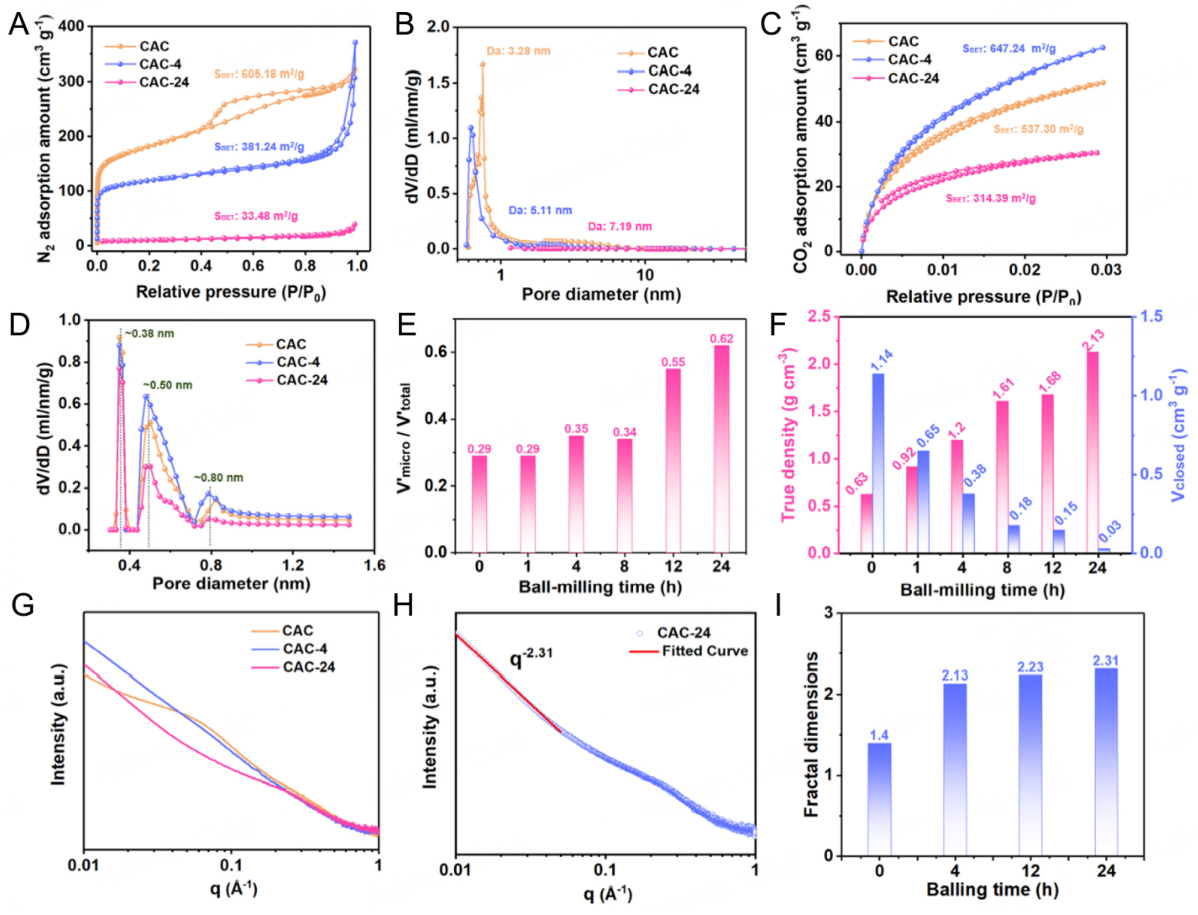

Figure 3. Pore structure characterizations. (A) N_2 adsorption-desorption isotherms of CAC, CAC-4 and CAC-24. (B) Pore size distribution of CAC, CAC-4 and CAC-24 by N_2 adsorption test. (C) CO_2 adsorption-desorption isotherms of CAC, CAC-4 and CAC-24. (D) Pore size distribution of CAC, CAC-4 and CAC-24 by CO_2 adsorption test. (E) Micropore volume ratio of CAC-*x*. (F) True density and closed pore volume of CAC, CAC-4 and CAC-24. (G) SAXS patterns of CAC, CAC-4 and CAC-24. (H) Fitted SAXS pattern of CAC-24 in the low-q range. (I) Fractal dimensions of CAC-*x*.

CAC to 2.13 g cm^{-3} for CAC-24), indicating a significant decrease in the closed pore volume. Therefore, it can be inferred that the ball milling process can eliminate or transform the closed pores in the activated carbon into open ones, improve the density of the materials and facilitate the high-density storage and transportation of ions. In addition, the fractal dimensions of CAC, CAC-4 and CAC-24 were fitted by SAXS characterization by which the cross-linking degrees of pores can be revealed. Figure 3G shows the SAXS overall scans of CAC, CAC-4 and CAC-24, from which these samples present typical structure characteristics of porous carbon materials. Therein, CAC possesses an obvious peak around 0.1 $Å^{-1}$, indicating high content of closed pores in the structure[55]. The intensity values of peaks around 0.1 $Å^{-1}$ of CAC-*x* decrease with the extension of ball milling time, indicating a gradual decrease in the content of closed pores[43]. Pore structure evolution and development process is further characterized by pore fractal dimension fitting which can help understand the fractal information of the pore network[56-58]. The calculated pore fractal dimension including open pores and closed pores can be used to describe the surface roughness of pore structure (surface fractal, $3 < P < 4$ in which P represents the slope of the fitted line) or the aggregation of smaller pore network (pore fractal, $1 < P < 3$)[56,59]. The fractal dimensions of mesopores from SAXS tests are presented in Figure 3H and I, Supplementary Figure 19. Specifically, the value of fractal dimension is 1.40 for CAC, which becomes higher to 2.31 for CAC-24 with the extension of ball milling

time. As reported in the literature[56,60], when the fractal dimension increases closer to 3, it indicates that pores are distributed in a network of pore clusters of a particular size that become more sponge-like and branched during the ball milling process. Therefore, it can be concluded from the pore fractal analysis that the mechanical force in ball milling process could transform the sheet-like pore structure in pristine CAC into a more three-dimensional and cross-linked pore network in CAC-*x*.

In this paper, low-cost coal with wide sources and high carbon content was used as the initial carbon source, and through the physical activation process of CO_2 gas mild etching, the initial coal was transformed into porous carbon materials with rich pore structure. The formation of pores leads to the decrease of material skeleton density. In order to increase the material density and simultaneously optimize the multi-scale structure of the material to make it conducive to the high-density storage of ions, the mechanical ball milling process was adopted to realize the reconstruction of the full-scale structures of the material through the high-speed impact of the balls on the material. The synthesis process is environmentally friendly and convenient to operate, which has the value of popularization.

The evolution mechanism of pore structure of CAC during ball milling can be depicted, as shown in Figure 4. The original CAC was obtained through the CO_2 activation process, in which CO_2 molecules react with the coal skeleton from the outside to the inside. CO_2 activation process causes local etching to form porous channels filled with micropores and meso-/macro- pore clusters, which finally form a porous network with low fractal dimension. The pores of CAC are mainly composed of intragranular pores (micropores) and interparticle pores (meso-/macro- pores). In addition, there are a large number of ineffective closed pores inside the material. After the treatment of ball milling within a short period of time (less than 4 h in our study), the ineffective interparticle pores of CAC are eliminated with particle size decreasing. At the same time, the ineffective closed pores are transformed to open pores under the action of mechanical shear force, resulting in a significant increase in fractal dimension of CAC-24. Benefitting from the elimination of ineffective pores, the densities of CAC-*x* increase and the pores become more cross-linked and three-dimensional.

Electrochemical performance in a three-electrode system

Hereto, we have demonstrated that mechanochemistry can profoundly alter the multi-scale structure of activated carbon, especially in eliminating the ineffective pores and increasing the skeleton density of activated carbon. Next, the supercapacitor performances of obtained CAC-*x* were evaluated with emphasis on examining the volumetric capacitance and energy density. Initially, in a three-electrode setup with 6M KOH aqueous solution serving as the electrolyte, CV curves at varying scan rates and GC profiles at different current densities were recorded [Supplementary Figures 20 and 21]. As depicted in Figure 5A, the CV curve of CAC-24 exhibits a larger integrated area compared to the other samples, hinting at its superior gravimetric capacitance. Furthermore, the deviation from a perfect rectangular shape in the CV curves suggests the contribution of pseudocapacitance. For the GC tests conducted at a current density of 0.5 A g^{-1} within the potential window of -1 to 0 V *vs.* the SCE, as shown in Figure 5B, CAC-24 demonstrates the longest discharge duration. Similarly, the charge-discharge curves are not strictly triangular, indicating that ions are not completely stored in the form of electric double-layers, which is consistent with the conclusion of Figure 5A. Furthermore, the first-cycle Coulombic efficiency of the CAC-24 electrode at various current densities has been investigated, with results shown in Supplementary Figure 22. At a low current density of 0.5 A g^{-1}, oxygen-containing functional groups of CAC-24 may undergo side reactions with the electrolyte, leading to incomplete discharge. However, as the current density increases, the electrochemical process is predominantly influenced by the adsorption behavior, thereby leading to an increase in Coulombic efficiency. Figure 5C shows the CV curves of CAC-24 at various scan rates from 10 to 1,000 mV s^{-1}. Further, the specific gravimetric capacitances of CAC-*x* at different current densities calculated based on GC curves

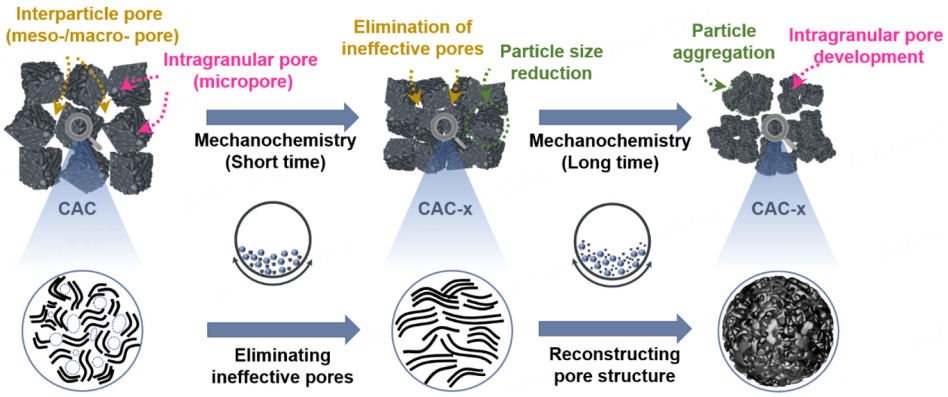

Figure 4. Schematic illustration of pore structure evolution of CAC-*x* during mechanochemistry process.

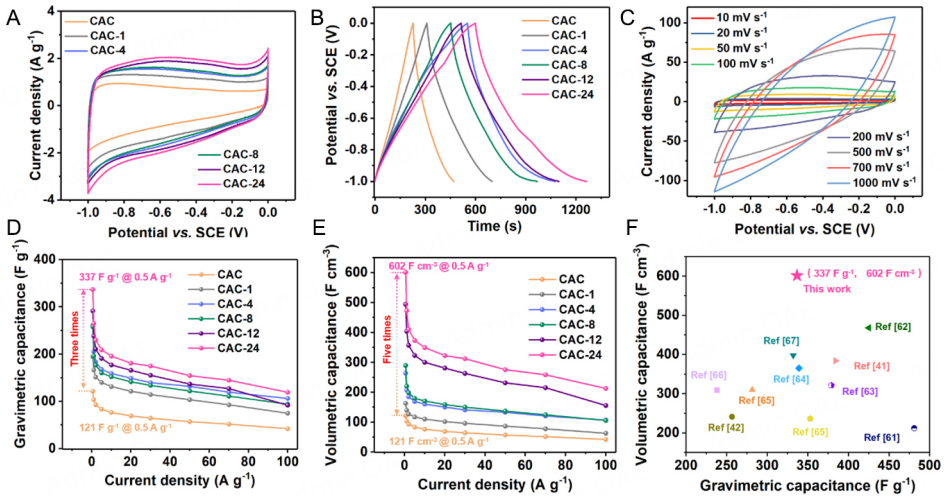

Figure 5. Electrochemical performances of CAC and CAC-*x* electrodes in a three-electrode system using 6M KOH as electrolyte. (A) CV curves at 10 mV s^{-1} and (B) GC curves at 0.5 A g^{-1} of CAC and CAC-*x*. (C) CV curves of CAC-24 at various scan rates from 10 mV s^{-1} to 1,000 mV s^{-1}. (D) Gravimetric capacitances of CAC-*x* calculated from GC curves. (E) Volumetric capacitances of CAC-*x* based on material skeleton densities. (F) Comparison of the volumetric and gravimetric capacitances of CAC-24 electrode with other reported carbon electrodes.

and at various scan rates calculated based on CV curves were respectively shown in Figure 5D and Supplementary Figure 23, showing that the specific gravimetric capacitances gradually increase with the ball milling time. Notably, although mechanical ball milling process reduces the overall porosity and specific surface area of activated carbon, the obtained CAC-*x* samples exhibit higher specific capacitances than pristine CAC. Particularly, the specific surface area of CAC-24 is only 33 m^2 g^{-1}, but the specific gravimetric capacitance is calculated to be 337 F g^{-1} at the current density of 0.5 A g^{-1}, which is nearly three times that of CAC (121 F g^{-1}). As expected, the volumetric capacitances based on material skeleton density (ρ_M) and electrode density (ρ_E) were calculated as given in Figure 5E, Supplementary Figures 24 and 25, Supplementary Table 5, from which the volumetric capacitances of CAC-*x* are greatly improved compared to pristine CAC. Notably, the volumetric capacitances of CAC-24 are up to 602 F cm^{-3} (based on ρ_M) and 390 F cm^{-3} (based on ρ_E), which are five times those of pristine CAC and are also located at the highest level among the reported porous carbon electrodes in similar systems[41,42,61-67] [Figure 5F and Supplementary Table 6].

To further elucidate the ion storage mechanism, the relative contributions of the capacitive-controlled and diffusion-controlled charge storage of CAC and CAC-*x* have been calculated. Quantitative charge storage can be obtained according to[68]

$$i = av^b \tag{11}$$

where i and v are the peak current and the scan rate of CV curves, respectively, and a and b are adjustable parameters[69]. As shown in Supplementary Figure 26, the corresponding b value of CAC is calculated to be 0.866, indicating that the storage process of ions in CAC electrode follows a typical capacitive-controlled storage behavior[70]. However, the b values change with the increase of ball milling time, indicating that mechanochemical process changes the ions storage mechanism by reconstructing the multi-scale structure of material, as shown in Supplementary Figure 27. Additionally, the quantification accuracy of the ratios of diffusion- to capacitive-controlled processes was improved by[71]

$$i = k_1 v + k_2 v^{1/2} \tag{12}$$

$$\frac{i}{v^{1/2}} = k_1 v^{1/2} + k_2 v \tag{13}$$

where k_1 and k_2 are constants that can be calculated from CV curves at different scan rates.

As can be seen from Supplementary Figure 28, the calculated contributions of capacitive-controlled and diffusion-controlled ion storage processes of CAC-*x* samples indicate that the diffusion-controlled ratios of CAC-*x* first decrease from 42% for CAC to 37% for CAC-8 and then increase to 45% for CAC-24. Further analysis of the correlation between the capacitances and pore parameters reveals a highly positive correlation between the specific gravimetric capacitances and the proportions of micropore volume in CAC-*x* (V'_{micro}/V'_{total} shown in Figure 3E).

To further demonstrate the contributions of oxygen atoms to capacitances, the samples of CAC, CAC-4 and CAC-24 have been annealed at 800 °C for 1 h in hydrogen-argon mixture atmosphere to remove oxygen atoms in the material, and the obtained samples were noted as CAC-H, CAC-4H and CAC-24H, respectively. As shown in Supplementary Figure 29A and B, after mild treatment by H_2 reduction, CV curves of CAC-H have the largest area at various scan rates, while the area of CV curves of CAC-4H and CAC-24H are significantly reduced. It can also be seen from Supplementary Figure 29C and D that the GC curves of CAC-H have the longest discharge time at different current densities. Further, the specific gravimetric and volumetric capacitances of CAC-H, CAC-4H and CAC-24H at various scan rates were calculated. As presented in Supplementary Figure 29E and F, CAC-H has the highest specific gravimetric capacitances due to its high specific surface area and pore volume, while CAC-4H and CAC-24H have almost the same specific capacitances although their specific surface area and pore volume are more than ten times different. Therefore, it can be inferred that, in addition to the pseudocapacitances caused by the doped oxygen atoms, the optimization of the pore structure also has an important contribution to the capacitances.

Therefore, based on the above analyses of pore evolution pathway, although mechanical ball milling reduces the overall specific surface area and pore volume of activated carbon, the optimization of pore network, the increase in the proportions of micropore volume and the introduction of oxygen atoms in the ball milling process significantly improve the ion storage and transportation dynamics, endowing the CAC-24 with improved gravimetric capacitances. More importantly, the dense carbon skeleton of CAC-*x* can make great improvements in the volumetric capacitances.

Electrochemical performance in symmetrical supercapacitors

To delve deeper into the electrochemical characteristics of CAC-*x*, a set of two-electrode symmetrical supercapacitors were constructed using 6M KOH as the electrolyte. Figure 6A and Supplementary Figure 30 showcase the CV curves of the CAC-*x*-based symmetrical supercapacitors at different scan rates, from which the CV curves in the voltage window ranging from 0-1.0 V present approximately rectangular structure and there are no significant redox peaks, indicating the typical capacitive behavior. Figure 6B and Supplementary Figure 31 show the GC curves of CAC-*x*-based symmetrical supercapacitors at various current densities, from which the GC curves present symmetrical triangles at various current densities. The first-cycle Coulombic efficiency of the CAC-24-based symmetric supercapacitors at various current densities has been investigated, with results shown in Supplementary Figure 32. As higher current densities, the adsorption behavior primarily governs the electrochemical process, resulting in improved Coulombic efficiency. In comparison, the Coulombic efficiency of symmetric supercapacitors is higher than that of three-electrode systems, possibly because the two electrodes of symmetric supercapacitors are identical in structure and material, which can reduce internal resistance and polarization during charging and discharging processes. Figure 6C and D shows the Ragone plots of the gravimetric and volumetric energy densities and power densities for the CAC-*x*-based symmetrical supercapacitors at different current densities. As can be seen, both the gravimetric and volumetric energy densities of CAC-*x*-based symmetrical supercapacitors are higher than those of pristine CAC-based symmetrical supercapacitors at the same power densities. Furthermore, relations of the capacitance, energy density, and power density in terms of mass and volume are shown in Supplementary Figure 33. Due to its highest capacitance and density, the CAC-24-based symmetrical capacitor possesses the highest gravimetric energy density and volumetric energy density. The conductivity and electrochemical reaction kinetics of CAC-*x* electrodes were evaluated from the electrochemical impedance spectroscopy (EIS) spectra as shown in Supplementary Figure 34. The z' axis intercept and the semicircle diameter at high frequency are related to the intrinsic ohmic resistance (Rs) and the charge-transfer resistance (Rct), respectively, while the slope of the oblique line at a low frequency represents the diffusion impedance. Due to the more suitable and cross-linked pore structure distribution characteristics, CAC-24 has the smallest Rs, Rct and ion diffusion impedance, which results in excellent electrochemical properties. In addition, the EIS profiles of CAC and CAC-24 obtained before and after CV and GC tests were compared as shown in Supplementary Figure 35. Compared with the EIS profiles before CV and GC tests, the slope of the oblique line at a low frequency of CAC decreased after CV and GC tests, indicating an increase in ion diffusion resistance. For CAC-24, ion diffusion resistance was almost constant whether before or after the CV and GC tests, which may be due to the more connected pore structure.

For the volumetric energy storage characteristics emphasized in this work, the CAC-24 symmetrical supercapacitor delivers a maximum volumetric energy density up to 11.32 Wh L^{-1} based on skeleton density of the active material when the volumetric power density is 223 W L^{-1} [Figure 6E], which is higher than those of the reported aqueous supercapacitors constructed by activated carbon or porous carbon[42,61-64,66,67]. Even at a high power output of 4.36 kW L^{-1}, the volumetric energy density can still maintain 8.48 Wh L^{-1}, demonstrating an excellent rate performance. Figure 6F further shows the cycling stability of CAC-24-based symmetrical supercapacitors at the current density of 5 A g^{-1}, which demonstrates an outstanding long-term cycling stability with 85% capacitance retention after 30,000 cycles compared with other carbon-based symmetric supercapacitors in Supplementary Table 7. The above electrochemical tests manifest that simple mechanochemical post-treatment modification is an effective method for optimizing multi-scale structure, with a focus on eliminating ineffective pores to achieve pore reconstruction and material density improvement, thereby significantly improving the volumetric energy storage performances of carbon-based

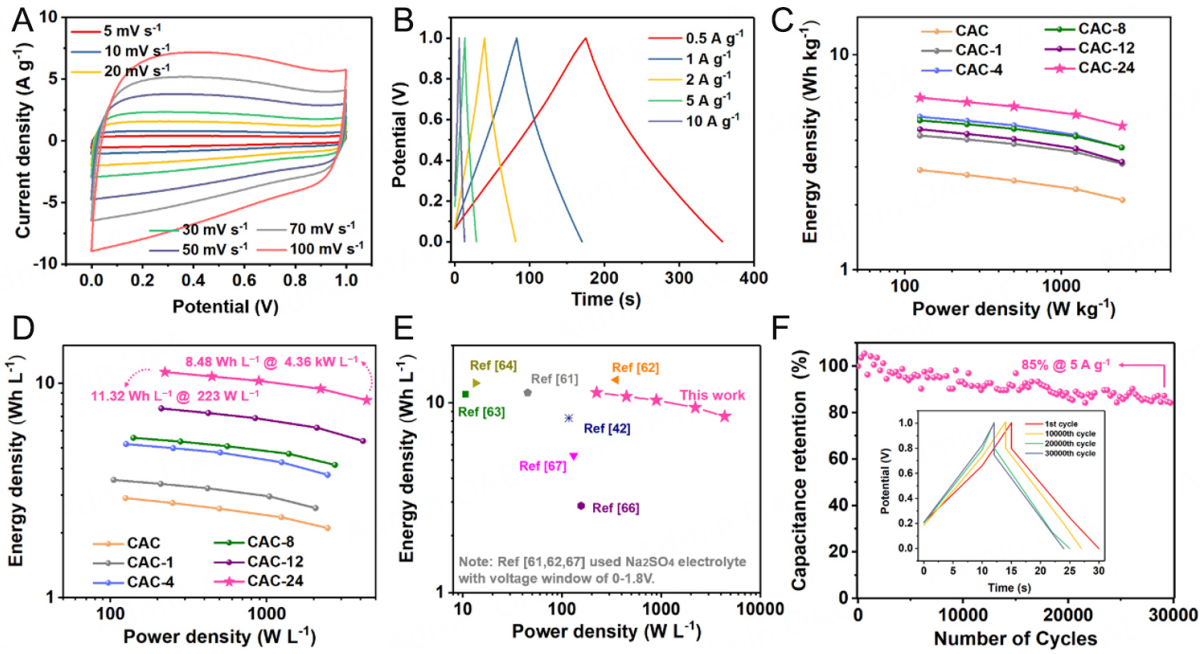

Figure 6. Electrochemical performances of symmetric supercapacitors using 6M KOH as electrolyte. (A) CV curves at various scan rates of CAC-24-based symmetric supercapacitors in 6M KOH aqueous solution. (B) GC curves at various current densities of CAC-24-based symmetric supercapacitors. (C) Gravimetric energy densities of CAC and CAC-*x*-based symmetric supercapacitors. (D) Volumetric energy densities of CAC and CAC-*x*-based symmetric supercapacitors calculated by material skeleton densities. (E) Ragone plots of CAC-24-based symmetric supercapacitors compared to some reported carbon-based supercapacitors in aqueous systems. (F) Cycling performance at 5 A g^{-1} of CAC-24-based symmetric supercapacitor.

porous electrodes. In addition, the electrochemical performances of CAC-*x*-based symmetrical supercapacitors assembled with $EMIMBF_4$ as electrolytes with voltage windows ranging from 0-3.6 V have also been tested with results shown in Supplementary Figures 36-38. Different from the results in aqueous systems, it is not the CAC-24 with the longest ball milling time that shows the best gravimetric and volumetric performances simultaneously. Among the obtained CAC-*x*, CAC-4-based symmetrical supercapacitors have the highest gravimetric energy density of 34 Wh kg^{-1}, while CAC-24-based symmetrical supercapacitors have the highest volumetric energy density of 42.3 Wh L^{-1} due to their high density. It may be due to the mismatch between the ultra-micro pores of CAC-24 and the ions in the ionic liquid system. It implies that pore structure optimization by mechanochemical modification should match the target ions in the electrolyte.

CONCLUSION

In summary, we report that the multi-scale structure of activated carbon can be adjusted by a simple mechanical ball milling post-treatment method, and the deep optimization of the pore structure has been achieved. Ineffective pores such as intergranular and closed pores were eliminated to achieve higher proportions of micropore volume in the total pore volume, more cross-linked pore structure distribution and higher material density, simultaneously. In addition, oxygen atoms introduced by the ball milling process also contribute to the pseudocapacitances. The obtained dense carbon material has a higher volumetric specific capacitance of up to 602 F cm^{-3} at 0.5 A g^{-1} with an ultra-low specific surface area of 33 m^2 g^{-1}. The aqueous symmetric supercapacitor assembled with 6M KOH as the electrolyte delivers a maximum volumetric energy density of 11.32 Wh L^{-1} when the volumetric power density is 223 W L^{-1}. This work proposes a simple and universal post-treatment method to optimize the pore structure of porous carbon for compact energy storage.

DECLARATIONS

Acknowledgments

The authors acknowledge the financial support from the National Natural Science Foundation of China and the Huaneng Group headquarters science and technology project.

Authors' contributions

Investigation, methodology, writing - original draft, writing - review & editing: Wu, D.
Made substantial contributions to the conception and design of the study and provided administrative, technical, and material support: Sun, F.; Li, Y.; Gao, J.; Zhao, G.
Performed data analysis and interpretation: Wang, H.; Zhang, B.
Conducted data acquisition: Yang, C.; Wang, Z.

Availability of data and materials

The data that support the findings of this study can be found in the Supplementary Materials of this article.

Financial support and sponsorship

This work is funded by the National Natural Science Foundation of China (Grant Nos. U21A20143 and 52322607) and Huaneng Group headquarters science and technology project (Grant No. HNKJ21-H32, Research on the key technologies for the preparation of coal-based graphene-like supercapacitor carbon materials).

Conflicts of interest

All authors declared that there are no conflicts of interest.

Ethical approval and consent to participate

Not applicable.

Consent for publication

Not applicable.

REFERENCES

1. Dong, D.; Xiao, Y. Recent progress and challenges in coal-derived porous carbon for supercapacitor applications. *Chem. Eng. J.* **2023**, *470*, 144441. DOI
2. Ciszewski, M.; Koszorek, A.; Radko, T.; Szatkowski, P.; Janas, D. Review of the selected carbon-based materials for symmetric supercapacitor application. *J. Electron. Mater.* **2019**, *48*, 717-44. DOI
3. Wang, Y.; Zhang, L.; Hou, H.; et al. Recent progress in carbon-based materials for supercapacitor electrodes: a review. *J. Mater. Sci.* **2021**, *56*, 173-200. DOI
4. Yan, D.; Liu, L.; Wang, X.; Xu, K.; Zhong, J. Biomass-derived activated carbon nanoarchitectonics with hibiscus flowers for high-performance supercapacitor electrode applications. *Chem. Eng. Technol.* **2022**, *45*, 649-57. DOI
5. Chen, H.; Liu, D.; Shen, Z.; Bao, B.; Zhao, S.; Wu, L. Functional biomass carbons with hierarchical porous structure for supercapacitor electrode materials. *Electrochim. Acta.* **2015**, *180*, 241-51. DOI
6. Shi, M.; Xin, Y.; Chen, X.; et al. Coal-derived porous activated carbon with ultrahigh specific surface area and excellent electrochemical performance for supercapacitors. *J. Alloys. Compd.* **2021**, *859*, 157856. DOI
7. Dong, D.; Zhang, Y.; Xiao, Y.; Wang, T.; Wang, J.; Gao, W. Oxygen-enriched coal-based porous carbon under plasma-assisted $MgCO_3$ activation as supercapacitor electrodes. *Fuel* **2022**, *309*, 122168. DOI
8. Yuan, Y.; Yi, R.; Sun, Y.; et al. Porous activated carbons derived from *Pleurotus eryngii* for supercapacitor applications. *J. Nanomater.* **2018**, *2018*, 1-10. DOI
9. Zheng, L.; Chen, M.; Liang, S.; Lü, Q. Oxygen-rich hierarchical porous carbon derived from biomass waste-kapok flower for supercapacitor electrode. *Diam. Relat. Mater.* **2021**, *113*, 108267. DOI

10. Qie, L.; Chen, W.; Xu, H.; et al. Synthesis of functionalized 3D hierarchical porous carbon for high-performance supercapacitors. *Energy. Environ. Sci.* **2013**, *6*, 2497. DOI
11. Ouyang, J.; Wang, X.; Wang, L.; et al. Construction of a porous carbon skeleton in wood tracheids to enhance charge storage for high-performance supercapacitors. *Carbon* **2022**, *196*, 532-9. DOI
12. Tang, D.; Hu, S.; Dai, F.; et al. Self-templated synthesis of mesoporous carbon from carbon tetrachloride precursor for supercapacitor electrodes. *ACS. Appl. Mater. Interfaces.* **2016**, *8*, 6779-83. DOI
13. Ren, M.; Zhang, C.; Wang, Y.; Cai, J. Development of N-doped carbons from zeolite-templating route as potential electrode materials for symmetric supercapacitors. *Int. J. Miner. Metall. Mater.* **2018**, *25*, 1482-92. DOI
14. Zhao, Y.; Zhang, Z.; Ren, Y.; et al. Vapor deposition polymerization of aniline on 3D hierarchical porous carbon with enhanced cycling stability as supercapacitor electrode. *J. Power. Sources.* **2015**, *286*, 1-9. DOI
15. He, S.; Hou, H.; Chen, W. 3D porous and ultralight carbon hybrid nanostructure fabricated from carbon foam covered by monolayer of nitrogen-doped carbon nanotubes for high performance supercapacitors. *J. Power. Sources.* **2015**, *280*, 678-86. DOI
16. Zhang, Z.; Mu, S.; Zhang, B.; et al. A novel synthesis of carbon nanotubes directly from an indecomposable solid carbon source for electrochemical applications. *J. Mater. Chem. A.* **2016**, *4*, 2137-46. DOI
17. Mhamane, D.; Aravindan, V.; Kim, M.; et al. Silica-assisted bottom-up synthesis of graphene-like high surface area carbon for highly efficient ultracapacitor and Li-ion hybrid capacitor applications. *J. Mater. Chem. A.* **2016**, *4*, 5578-91. DOI
18. Xu, Z.; Li, Z.; Holt, C. M.; et al. Electrochemical supercapacitor electrodes from sponge-like graphene nanoarchitectures with ultrahigh power density. *J. Phys. Chem. Lett.* **2012**, *3*, 2928-33. DOI
19. Panda, P.; Barman, S. A bottom-up fabrication for sulphur (S), nitrogen (N) co-doped two-dimensional microporous carbon nanosheets for high-performance supercapacitors and H_2, CO_2 storage. *Sustain. Energy. Fuels.* **2023**, *7*, 2441-54. DOI
20. Xia, K.; Gao, Q.; Jiang, J.; Hu, J. Hierarchical porous carbons with controlled micropores and mesopores for supercapacitor electrode materials. *Carbon* **2008**, *46*, 1718-26. DOI
21. Jiang, L.; Wang, J.; Li, Y.; et al. Facile synthesis of three-dimensional carbon nanocages with hierarchical porous structures as supercapacitor electrode materials. *Int. J. Electrochem. Sci.* **2019**, *14*, 5950-60. DOI
22. Li, Y. H.; Zhang, S. Y.; Yu, Q. M. Hierarchical porous materials for supercapacitors. *Adv. Mater. Res.* **2013**, *750-2*, 894-8. DOI
23. Zhou, Y.; Song, Z.; Hu, Q.; et al. Hierarchical nitrogen-doped porous carbon/carbon nanotube composites for high-performance supercapacitor. *Superlattices. Microstruct.* **2019**, *130*, 50-60. DOI
24. Wang, L.; Jia, M.; Lu, W.; et al. A facile route for preparation of high-performance hierarchical porous carbons for supercapacitor electrodes. *Int. J. Electrochem. Sci.* **2016**, *11*, 6052-63. DOI
25. Chmiola, J.; Yushin, G.; Gogotsi, Y.; Portet, C.; Simon, P.; Taberna, P. L. Anomalous increase in carbon capacitance at pore sizes less than 1 nanometer. *Science* **2006**, *313*, 1760-3. DOI PubMed
26. Zhang, S.; Zhu, J.; Qing, Y.; et al. Ultramicroporous carbons puzzled by graphene quantum dots: integrated high gravimetric, volumetric, and areal capacitances for supercapacitors. *Adv. Funct. Mater.* **2018**, *28*, 1805898. DOI
27. Li, Q.; Jiang, Y.; Jiang, Z.; et al. Ultrafast pore-tailoring of dense microporous carbon for high volumetric performance supercapacitors in organic electrolyte. *Carbon* **2022**, *191*, 19-27. DOI
28. Li, Z.; Gadipelli, S.; Li, H.; et al. Tuning the interlayer spacing of graphene laminate films for efficient pore utilization towards compact capacitive energy storage. *Nat. Energy.* **2020**, *5*, 160-8. DOI
29. Tao, Y.; Xie, X.; Lv, W.; et al. Towards ultrahigh volumetric capacitance: graphene derived highly dense but porous carbons for supercapacitors. *Sci. Rep.* **2013**, *3*, 2975. DOI PubMed PMC
30. Yang, T.; Cao, Y.; Yu, Y.; et al. Kinetic enhanced bio-derived porous carbon tile laminate paper for ultrahigh-rate supercapacitors. *J. Power. Sources.* **2022**, *525*, 231148. DOI
31. Rani, J. R.; Thangavel, R.; Oh, S. I.; et al. High volumetric energy density hybrid supercapacitors based on reduced graphene oxide scrolls. *ACS. Appl. Mater. Interfaces.* **2017**, *9*, 22398-407. DOI
32. Ruike, M.; Kasu, T.; Setoyama, N.; Suzuki, T.; Kaneko, K. Inaccessible pore characterization of less-crystalline microporous solids. *J. Phys. Chem.* **1994**, *98*, 9594-600. DOI
33. Kierzek, K.; Gryglewicz, G. Activated carbons and their evaluation in electric double layer capacitors. *Molecules* **2020**, *25*, 4255. DOI PubMed PMC
34. Zheng, Y.; Wan, Y.; Chen, J.; Chen, H.; Gao, B. MgO modified biochar produced through ball milling: a dual-functional adsorbent for removal of different contaminants. *Chemosphere* **2020**, *243*, 125344. DOI PubMed PMC
35. Zhao, L. Y.; Dong, X. L.; Chen, J. Y.; Lu, A. H. A mechanochemical-assisted synthesis of boron, nitrogen co-doped porous carbons as metal-free catalysts. *Chemistry* **2020**, *26*, 2041-50. DOI PubMed
36. Sun, F.; Qu, Z.; Gao, J.; et al. In situ doping boron atoms into porous carbon nanoparticles with increased oxygen graft enhances both affinity and durability toward electrolyte for greatly improved supercapacitive performance. *Adv. Funct. Mater.* **2018**, *28*, 1804190. DOI
37. Sun, F.; Wang, H.; Qu, Z.; et al. Carboxyl-dominant oxygen rich carbon for improved sodium ion storage: synergistic enhancement of adsorption and intercalation mechanisms. *Adv. Energy. Mater.* **2021**, *11*, 2002981. DOI
38. Zhao, L. Y.; Dong, X. L.; Lu, A. H. Mechanochemical synthesis of porous carbons and their applications in catalysis. *Chempluschem* **2020**, *85*, 866-75. DOI PubMed
39. Xuan, M.; Schumacher, C.; Bolm, C.; Göstl, R.; Herrmann, A. The mechanochemical synthesis and activation of carbon-rich π-

conjugated materials. *Adv. Sci.* **2022**, *9*, e2105497. DOI PubMed PMC

40. Kumar, M.; Xiong, X.; Wan, Z.; et al. Ball milling as a mechanochemical technology for fabrication of novel biochar nanomaterials. *Bioresour. Technol.* **2020**, *312*, 123613. DOI
41. Yao, Y.; Ge, D.; Yu, Y.; et al. Filling macro/mesoporosity of commercial activated carbon enables superior volumetric supercapacitor performances. *Microporous. Mesoporous. Mater.* **2023**, *350*, 112446. DOI
42. Zhang, Y.; Fan, S.; Li, S.; Song, Y.; Wen, G. 3D porous oxygen-enriched graphene hydrogels with well-balanced volumetric and gravimetric performance for symmetric supercapacitors. *J. Mater. Sci.* **2020**, *55*, 12214-31. DOI
43. Tang, Z.; Zhang, R.; Wang, H.; et al. Revealing the closed pore formation of waste wood-derived hard carbon for advanced sodium-ion battery. *Nat. Commun.* **2023**, *14*, 6024. DOI PubMed PMC
44. Yuan, R.; Dong, Y.; Hou, R.; et al. Structural transformation of porous and disordered carbon during ball-milling. *Chem. Eng. J.* **2023**, *454*, 140418. DOI
45. Wu, D.; Sun, F.; Qu, Z.; et al. Multi-scale structure optimization of boron-doped hard carbon nanospheres boosting the plateau capacity for high performance sodium ion batteries. *J. Mater. Chem. A.* **2022**, *10*, 17225-36. DOI
46. Lee, S. H.; Kang, D. S.; Lee, S. M.; et al. X-ray diffraction analysis of the effect of ball milling time on crystallinity of milled polyacrylonitrile-based carbon fiber. *Carbon. Lett.* **2018**, *26*, 11-17. DOI
47. Lu, L.; Sahajwalla, V.; Kong, C.; Harris, D. Quantitative X-ray diffraction analysis and its application to various coals. *Carbon* **2001**, *39*, 1821-33. DOI
48. Dippel, B.; Jander, H.; Heintzenberg, J. NIR FT Raman spectroscopic study of flame soot. *Phys. Chem. Chem. Phys.* **1999**, *1*, 4707-12. DOI
49. Chang, Q.; Gao, R.; Li, H.; Yu, G.; Wang, F. Effect of CO_2 on the characteristics of soot derived from coal rapid pyrolysis. *Combust. Flame.* **2018**, *197*, 328-39. DOI
50. Le, K. C.; Pino, T.; Pham, V. T.; Henriksson, J.; Török, S.; Bengtsson, P. Raman spectroscopy of mini-CAST soot with various fractions of organic compounds: structural characterization during heating treatment from 25 °C to 1000 °C. *Combust. Flame.* **2019**, *209*, 291-302. DOI
51. Chen, C.; Huang, Y.; Zhu, Y.; et al. Nonignorable influence of oxygen in hard carbon for sodium ion storage. *ACS. Sustain. Chem. Eng.* **2020**, *8*, 1497-506. DOI
52. Luo, J.; Niu, Q.; Jin, M.; Cao, Y.; Ye, L.; Du, R. Study on the effects of oxygen-containing functional groups on Hg adsorption in simulated flue gas by XAFS and XPS analysis. *J. Hazard. Mate.* **2019**, *376*, 21-8. DOI
53. Gao, B.; Yap, P. S.; Lim, T. M.; Lim, T. Adsorption-photocatalytic degradation of acid red 88 by supported TiO_2: effect of activated carbon support and aqueous anions. *Chem. Eng. J.* **2011**, *171*, 1098-107. DOI
54. Kim, T.; Kim, D.; Ideta, K.; et al. Structural pore elucidation of super-activated carbon based on the micro-domain structure model. *J. Ind. Eng. Chem. Chem.* **2021**, *101*, 186-94. DOI
55. Au, H.; Alptekin, H.; Jensen, A. C. S.; et al. A revised mechanistic model for sodium insertion in hard carbons. *Energy. Environ. Sci.* **2020**, *13*, 3469-79. DOI
56. Liu, Y.; Paskevicius, M.; Sofianos, M. V.; Parkinson, G.; Li, C. In situ SAXS studies of the pore development in biochar during gasification. *Carbon* **2021**, *172*, 454-62. DOI
57. Beaucage, G. Determination of branch fraction and minimum dimension of mass-fractal aggregates. *Phys. Rev. E. Stat. Nonlin. Soft. Matter. Phys.* **2004**, *70*, 031401. DOI PubMed
58. Beaucage, G. Small-angle scattering from polymeric mass fractals of arbitrary mass-fractal dimension. *J. Appl. Crystallogr.* **1996**, *29*, 134-46. DOI
59. Pfeifer, P.; Ehrburger-Dolle, F.; Rieker, T. P.; et al. Nearly space-filling fractal networks of carbon nanopores. *Phys. Rev. Lett.* **2002**, *88*, 115502. DOI
60. Rennhofer, H.; Köhnke, J.; Keckes, J.; et al. Pore development during the carbonization process of lignin microparticles investigated by small angle X-ray scattering. *Molecules* **2021**, *26*, 2087. DOI PubMed PMC
61. Yan, J.; Wang, Q.; Lin, C.; Wei, T.; Fan, Z. Interconnected frameworks with a sandwiched porous carbon layer/graphene hybrids for supercapacitors with high gravimetric and volumetric performances. *Adv. Energy. Mater.* **2014**, *4*, 1400500. DOI
62. Long, C.; Jiang, L.; Wu, X.; et al. Facile synthesis of functionalized porous carbon with three-dimensional interconnected pore structure for high volumetric performance supercapacitors. *Carbon* **2015**, *93*, 412-20. DOI
63. Xie, Q.; Bao, R.; Zheng, A.; et al. Sustainable low-cost green electrodes with high volumetric capacitance for aqueous symmetric supercapacitors with high energy density. *ACS. Sustain. Chem. Eng.* **2016**, *4*, 1422-30. DOI
64. Xie, Q.; Chen, G.; Bao, R.; Zhang, Y.; Wu, S. Polystyrene foam derived nitrogen-enriched porous carbon/graphene composites with high volumetric capacitances for aqueous supercapacitors. *Microporous. Mesoporous. Mater.* **2017**, *239*, 130-7. DOI
65. Mo, R.; Zhao, Y.; Zhao, M.; et al. Graphene-like porous carbon from sheet cellulose as electrodes for supercapacitors. *Chem. Eng. J.* **2018**, *346*, 104-12. DOI
66. Wang, C.; Zhang, X.; Wang, J.; et al. Boron/nitrogen/oxygen co-doped carbon with high volumetric performance for aqueous symmetric supercapacitors. *J. Electrochem. Soc.* **2018**, *165*, A856-66. DOI
67. Ma, Y.; Zhang, X.; Liang, Z.; et al. B/P/N/O co-doped hierarchical porous carbon nanofiber self-standing film with high volumetric and gravimetric capacitance performances for aqueous supercapacitors. *Electrochim. Acta.* **2020**, *337*, 135800. DOI
68. Karuppasamy, K.; Vikraman, D.; Hussain, S.; et al. Unveiling the redox electrochemistry of MOF-derived fcc-NiCo@GC polyhedron

as an advanced electrode material for boosting specific energy of the supercapattery. *Small* **2022**, *18*, e2107284. DOI

69. Zhao, J.; Wang, Y.; Qian, Y.; et al. Hierarchical design of cross-linked $NiCo_2S_4$ nanowires bridged NiCo-hydrocarbonate polyhedrons for high-performance asymmetric supercapacitor. *Adv. Funct. Mater.* **2023**, *33*, 2210238. DOI
70. Zhou, Y.; Jia, Z.; Zhao, S.; et al. Construction of triple-shelled hollow nanostructure by confining amorphous Ni-Co-S/crystalline MnS on/in hollow carbon nanospheres for all-solid-state hybrid supercapacitors. *Chem. Eng. J.* **2021**, *416*, 129500. DOI
71. Liu, S.; Kang, L.; Hu, J.; et al. Realizing superior redox kinetics of hollow bimetallic sulfide nanoarchitectures by defect-induced manipulation toward flexible solid-state supercapacitors. *Small* **2022**, *18*, e2104507. DOI